JOURNAL OF AIRCRAFT
Vol. 42, No. 6, November–December 2005

Drag Prediction of Engine–Airframe Interference Effects with CFX-5

R. B. Langtry,* M. Kuntz,† and F. R. Menter‡
ANSYS CFX Germany, 83624 Otterfing, Germany

The commercial computational fluid dynamics (CFD) code CFX-5 of ANSYS, Inc., has been used to compute the engine installation drag for the German Aerospace Center (DLR) F6 aircraft configuration as part of the Second AIAA Drag Prediction Workshop. The computations were performed with the standard hexahedral meshes provided by ICEM-CFD to the workshop. The full drag polar for the DLR-F6 configuration has been computed. For all cases, good agreement between the experiment and the predictions were obtained for lift, drag, and pitching moment coefficients. All simulations where based on the shear stress transport turbulence model, and additional computations have indicated that turbulence modeling issues are largely responsible for the overprediction of the lift curve slope that was observed by many of the workshop participants.

Introduction

COMPUTATIONAL fluid dynamics (CFD) is now widely used in the aircraft industry to evaluate aerodynamic performance during the conceptual and preliminary design stages. With the recent advances in CFD and computer capabilities, it is now possible to simulate complete airplane configurations in a short enough period of time and to have a significant impact on the design cycle.

It is generally agreed that CFD is a valuable tool for evaluating the rate of change in the aerodynamic characteristics (such as drag or lift) due to design changes. However, there is still a significant amount of uncertainty about the accuracy of CFD for predicting the absolute value of the aerodynamic characteristics (particularly drag). As a result of this lack of confidence, the current state of the art is to use CFD as a tool for screening a large number of potential designs. The best candidates are then selected for further testing in a wind tunnel, where the actual values of the aerodynamic characteristics are measured and used for all of the performance calculations.

Because of the desire to reduce the design cycle time and minimize the costs associated with experimental validation, it is desirable to predict the absolute values of the aerodynamic characteristics. The goal of the Second AIAA Drag Prediction Workshop was, therefore, to assess the state of the art in CFD and to help increase the confidence in using this technology to predict the aerodynamic performance of a complex aircraft configuration.

The test case chosen for the workshop was the German Aerospace Center (DLR) F6 configuration with (wing body engine pylon, WBNP) and without engines (wing body, WB) mounted underneath the wing. This test case was selected because it is relatively complex and because there is a large body of experimental data available in the public domain.

Test Case Description

The DLR-F6 configuration represents a typical twin-engine wide-body aircraft. For a design cruise Mach number of 0.75, the design lift coefficient is 0.5 (Ref. 1). Figure 1 shows the geometry for the DLR-F6 configuration with the engine pylons/nacelles. For the workshop, the engines were represented by through-flow nacelles.

The experimental test campaigns were performed between 1993 and 1996 in the ONERA S2MA pressurized wind tunnel.[1] The model was sting mounted in the transonic test section, and the Mach number was varied between $Ma_\infty = 0.6$ and 0.8 while the Reynolds number (based on aerodynamic mean chord c) was held constant at $Re = 3 \times 10^6$. To represent flight conditions, transition strips were mounted on the wind-tunnel model. The strips were located at $x = 15$ mm on the fuselage nose and engine nacelle. On the wing, the strips were located as follows: lower wing root, kink, and tip, $x/c = 25\%$; and upper wing root, $x/c = 5\%$, kink $x/c = 15\%$, span $= 0.844$ $x/c = 15\%$, and tip x/c 5%.

For a Mach number of 0.75, the drag polar was measured for the DLR-F6 configuration with and without the engines at angles of attack from -5 to $+2$ deg. The workshop is based around four cases. Case 1 is a single-point grid refinement study for the DLR-F6 with and without the engine pylons at the design Mach number of 0.75 and a lift coefficient of 0.5. Three grids, coarse, medium, and fine, are required for a total of six simulations for case 1. The present results were computed with the standard ICEM Hexa grids provided by the workshop. For the WB configuration, the coarse, medium, and fine grids consisted of 3.5, 5.8, and 10.1 million nodes, whereas the WBNP configuration consisted of 4.9, 8.4, and 12.7 million nodes. Case 2 is a calculation of the drag polar with and without the engines using the two best practice grids determined in case 1. The required angles of attack for the drag polar are -3, -2, -1.5, -1.0, 0.0, 1.0, and 1.5 deg. Case 3 is a comparison between fully turbulent and transitional results for the design Mach number and lift coefficient. Case 4 is a systematic variation of the Mach number from 0.5 to 0.77 to calculate the transonic drag rise. Cases 1 and 2 are mandatory for the workshop, whereas cases 3 and 4 are optional. In the present study due to time constraints, only the mandatory cases have been completed.

Numerical Method

In CFX-5, the Reynolds averaged Navier–Stokes (RANS) equations are discretized using a vertex-based finite volume method, which is conservative and time implicit.[2,3] The computational hybrid and unstructured mesh can consist of different element types such as hexahedrals, prisms, wedges, and tetrahedrals. A control volume is constructed around each nodal point of the mesh, and the fluxes are computed at the integration points located at the subfaces between two control volumes. The discrete equations are evaluated using a bounded second-order advection scheme similar to that of Barth and Jesperson.[4] The mass flow is evaluated such that a pressure–velocity coupling is achieved via the Rhie and Chow[5] algorithm.

The discrete systems of equations are solved by the coupled algebraic multigrid method developed by Raw (see Ref. 3). The

Presented as Paper 2004-0392 at the AIAA 42nd Aerospace Sciences Meeting and Exhibit, Reno, NV, 5–8 January 2004; received 9 August 2004; revision received 16 March 2005; accepted for publication 17 March 2005.

*Engineer, Software Development Department. Member AIAA.
†Senior Engineer, Software Development Department.
‡Manager Scientific Coordination, Software Development Department. Member AIAA.

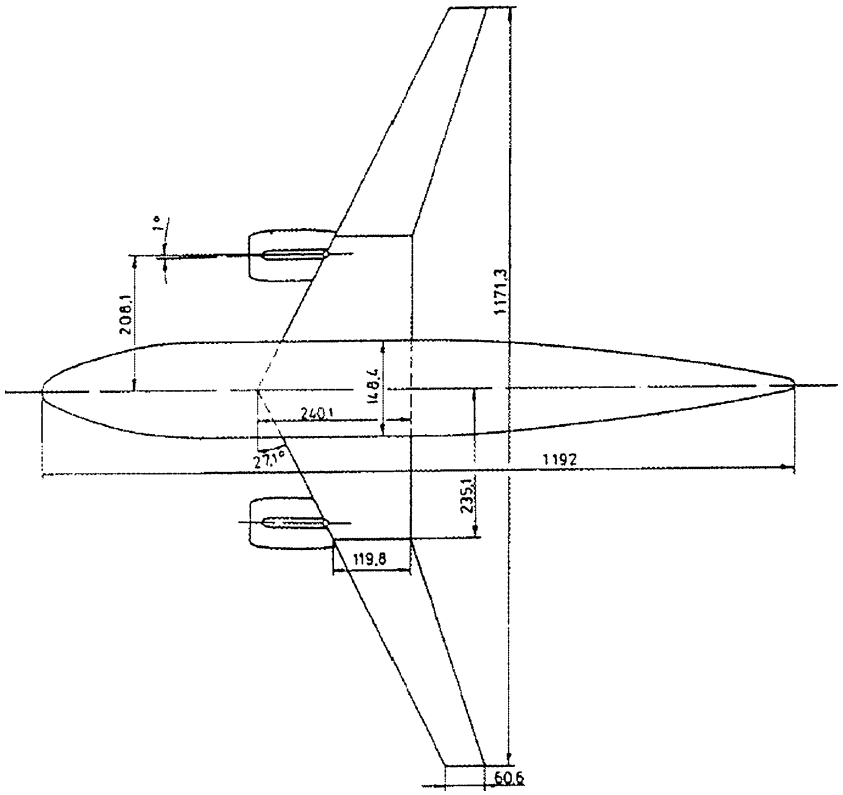

Fig. 1 DLR-F6 Geometry with mounted engine pylons wing reference area $S = 0.1453$ m^2 and aerodynamic mean chord $c = 0.1412$ m (reproduced from Brodersen and Stürmer[1]).

numerical effort of this method scales linearly with the number of grid nodes, which is selected to resolve the computational domain. Steady-state applications are computed by time step iteration until a user-defined convergence level is reached. For a transient computation, an iterative procedure updates the nonlinear coefficients within each time step (coefficient loop), whereas the outer loop advances the solution in time. The Reynolds stresses in the momentum equations are computed using the shear stress transport (SST) two-equation turbulence model[6] and an automatic wall treatment.[7]

To match the transition locations in the experiment, the production term in the turbulent kinetic energy equation of the SST model was set to zero upstream of the experimental transition location. Downstream of the transition location, the regular production term was used. This resulted in laminar flow on the wing upstream of the experimental trip locations and turbulent flow downstream of the trip location. No attempt was made to model transition on the leading edges of the fuselage or the engine nacelle.

Boundary Conditions and Time Integration

The boundary conditions used in the present simulations are as follows.

1) The inlet has specified velocities and turbulence quantities ($Tu = 0.1\%$ and $\mu_t/\mu = 1$).

2) There is automatic wall treatment for the walls (automatic shift from low Reynolds number model to wall functions based on grid spacing) For current grids, it operates in the low Reynolds number mode.

3) The boundary conditions at the outlet are average static pressure to match Mach number and Reynolds number.

4) The other boundaries are defined as openings (for incoming flow freestream conditions or outgoing flow static pressure).

It was observed in some of the simulations that an unsteady oscillation of the separation bubble at the wing–body junction was captured with small time steps ($\Delta t \sim 1 \times 10^{-5}$ s). This was also observed by some of the participants in the workshop. For this reason, the simulations have been carried out in unsteady mode using three coefficient loops. However, a relatively large time step was selected to damp the oscillation and to reduce the numerical effort ($\Delta t \sim 2 \times 10^{-4}$ s). The convergence of the lift and drag coefficients for a typical run can be seen in Fig. 2. The simulations typically converged in 120–150 time steps. The computing times per run were of the order of 20–24 h on a 16 processor AMD 1900 + Linux cluster for the 5.8 million node grid. Note that unsteady simulations with three coefficient loops have been performed. For steady-state simulations, a factor of 2–3 in CPU time reduction can be achieved.

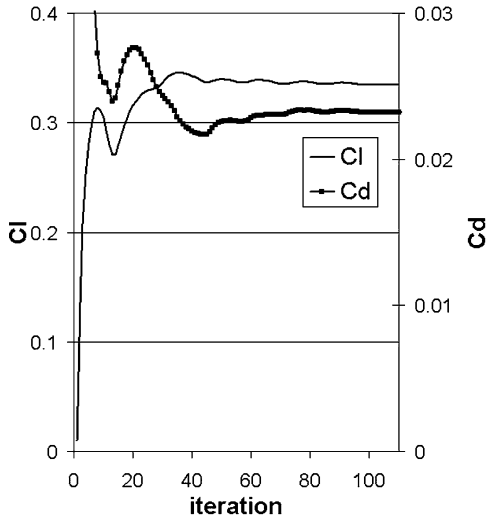

Fig. 2 Typical convergence history for lift and drag.

Results

The lift curve obtained from the case 2 simulations is shown in Fig. 3. For the configuration without engines (WB), the agreement between the experiment and CFX-5 is excellent. Near the design lift coefficient for the configuration with engine pylons (WBNP),

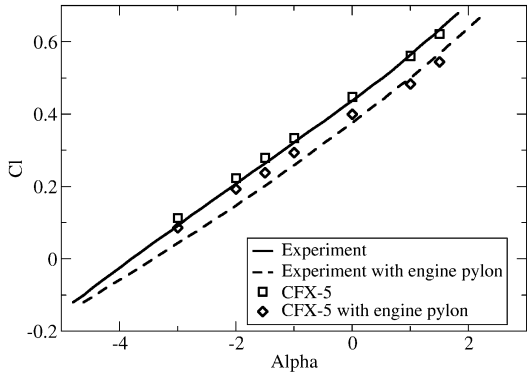

Fig. 3 Measured and computed lift curve slope (*Cl* vs alpha) for the DLR-F6 configuration without (WB) and with (WBNP) engine pylons.

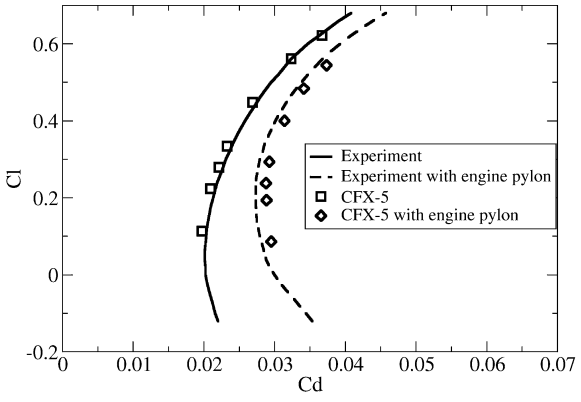

Fig. 4 Measured and computed drag polar (*Cl* vs *Cd*) for the DLR-F6 configuration without (WB) and with (WBNP) engine pylons.

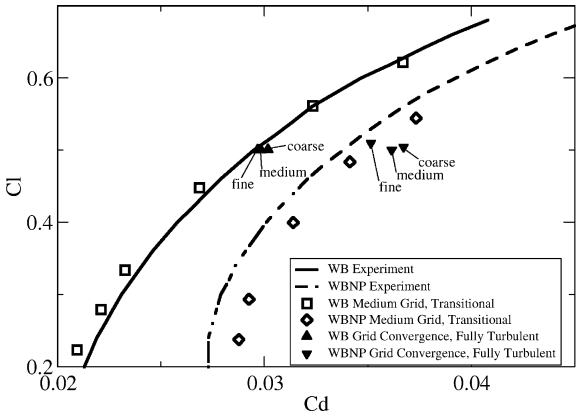

Fig. 5 Grid-convergence study for the drag polar (*Cl* vs *Cd*) of the DLR-F6 configuration without (WB) and with (WBNP) engine pylons.

the agreement between experiment and CFX-5 is also very good. However, at lower angles of attack, there is a noticeable difference between the two. At this point, it is not clear what has caused this; however, a similar trend has been observed with other CFD codes as well. It is possible that the difference has been caused by the somewhat artificial way the laminar zones were enforced in the CFD simulation. It is also possible that it could be an aeroelastic effect on the wind-tunnel model caused by the unloading of the wing at the negative angles of attack, and this effect on the geometry was not accounted for in the CFD simulations.

The drag polars obtained from the case 2 simulations are shown in Fig. 4. Again the agreement between experiments and CFX-5 is very good. The maximum error between experiment and the predictions for the configuration without engines is 3.2%, and with engines the maximum error is 5.5%. In Fig. 5, the predicted lift and drag coefficients from the grid-refinement study are compared to drag polar results. The grid-refinement study was performed fully turbulent without any laminar zones specified, and as a result, the drag is larger than the drag polar calculations. For both configurations, the predicted lift and drag approaches the experimental values as the grid is refined. The difference between the coarse, medium, and fine grids is much larger for the configuration with engine pylons. In fact, for the configuration with engine pylons, the difference between the medium and fine grid is approximately the same amount as the error between the experiment and the drag polar results (which were computed using the medium grid). It is, therefore, expected that if the drag polar results were computed on the fine grid the error between the prediction and the experiment would be further reduced. Note, however, that the grid-refinement study is not fully conclusive because the grids have not been refined by constant factors.

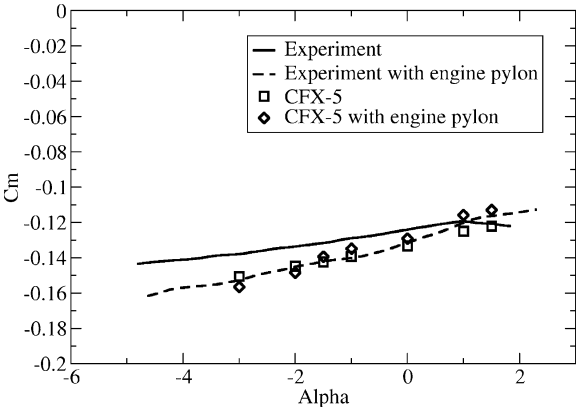

Fig. 6 Measured and predicted nose-down pitching moment (*Cm* vs alpha) for the DLR-F6 configuration without (WB) and with (WBNP) engine pylons.

The nose-down pitching moment coefficients obtained from case 2 are shown in Fig. 6. For the configuration, with engines, the agreement is very good. For the configuration without engines, the agreement is good at the design *Cl*, but at the lower angles of attack the CFD solution predicts a smaller difference between the two configurations then was observed in the experiment. At the First AIAA Drag Prediction Workshop, the pitching moment was by far the most difficult aerodynamic coefficient to calculate accurately. Most of the CFD codes significantly overpredicted the magnitude of the nose-down moment even though they successful calculated the lift and drag coefficients.[8] The fact that the CFX 5 prediction is reasonably close to the experiment for all three aerodynamic coefficients is very encouraging. It is believed that the pitching moment is the most sensitive quantity in the comparison with respect to grid resolution and that grid refinement will result in a further improvement in this quantity.

The pressure coefficient at various spanwise locations on the wing is shown in Fig. 7. In general, the agreement is very good compared to the experiments. However, the shock on the suction side of the wing does not appear to be quite as sharp as in the experiment. It is possible that the standard ICEM grids required further refinement in the wing region to capture the shocks correctly. As well, there does appear to be some differences in the leading-edge region between the experiment and the CFD predictions, and it is possible that this could be caused by transition. However, the pressure coefficient shown in Fig. 7 have been obtained for the fully turbulent case at the design lift coefficient of 0.5. This corresponds to an angle of attack of 0.51 deg, and unfortunately all the transitional computations in this study were made for the drag polar at the fixed angles of attack of -3, -2, -1.5, 0.0, 1.0, and 1.5 deg. As a result, a direct comparison between the fully turbulent and transitional pressure distribution, that is, case 3 from the workshop, was not possible due to time constraints.

The comparison between the experimental oil-flow visualization and the CFD predictions of the wing–body junction separation is shown in Fig. 8. Based on Fig. 8, it would appear that the CFD solution is overpredicting the size of the separation zones.

Alternatively, there could be some unsteadiness in the separated region in the wind tunnel. The present authors found that, if a small

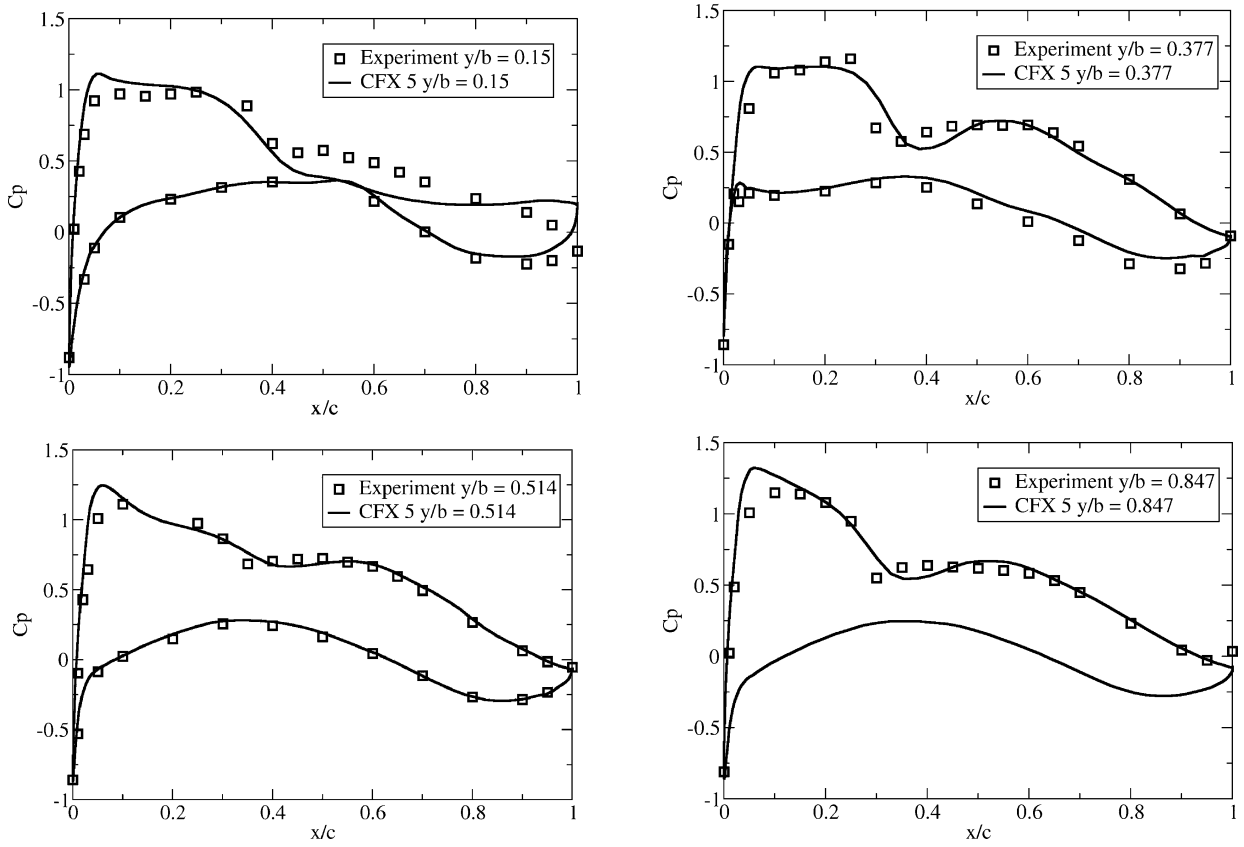

Fig. 7 Measured and calculated pressure coefficient *Cp* at 15 ($y/b = 0.15$), 37.7 ($y/b = 0.377$), 51.4 ($y/b = 0.514$), and 84.7% span ($y/b = 0.847$) for the DLR-F6 configuration with (WBNP) engine pylons.

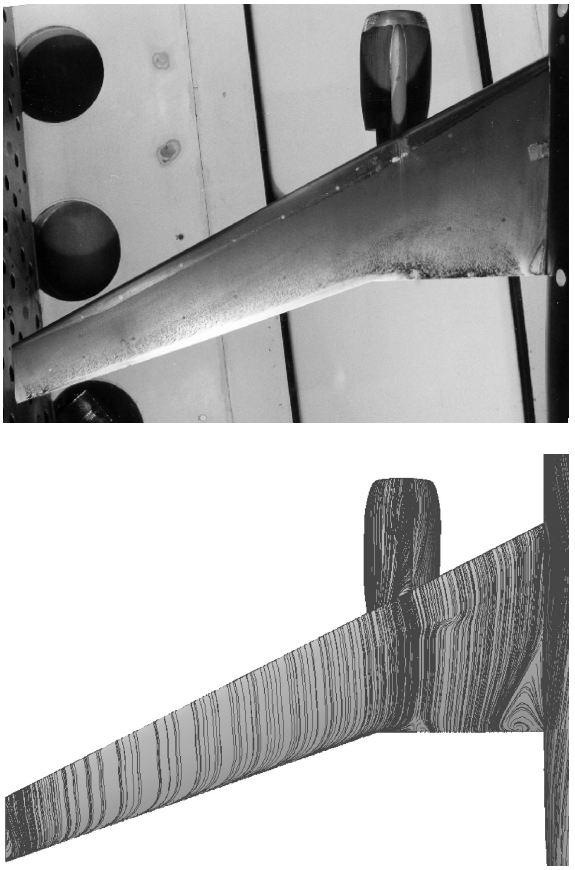

Fig. 8 Comparison between experimental oil-flow visualization (top) and CFD prediction (bottom) of the wing–body junction separation; note also separation near the wing kink.

enough time step was specified, the Navier–Stokes solution would predict some unsteadiness in the separated region. Because of the increased computing cost, this effect was not investigated in more detail. Note that there also appears to be a small separated region near the wing kink. This separation occurs in both the experiment and the CFD results, but it did not occur in the simulations when the engine was not present. Clearly the engine pylon has some local effect on the flow quality over that part of the wing, which results in a local trailing-edge separation.

The separation at the wing–pylon junction is shown in Fig. 9. Based on the predicted surface contour of isentropic Mach number, the presence of the engine appears to result in a local overspeed region where the flow underneath the wing goes supersonic. The subsequent deceleration results in a large separation at the wing–engine pylon corner. This separation was present in both the experiment and the simulation. However, based on the predicted isosurface of reverse flow, the separation appears to be larger in the simulation than in the experiment. This could potentially explain why in Fig. 4 the WBNP drag prediction was on average 5% higher than the experimental value. As well, the roughness strip on the wind-tunnel model was located very close to the separation location. Because roughness is known to energize the boundary layer, it is possible that the strip may have had some effect on the separation behavior, which is not captured by the CFD prediction.

The predicted surface contours of isentropic Mach number and skin friction for the WB and WBNP configurations are shown in Figs. 10 and 11. With the engine, there is a strong shock on the upper wing surface (Fig. 10). This in turn results in a small region of shock-induced separation (Fig. 11). As well, the engine pylon appears to have a very strong local effect on the flow quality on the upper wing surface. The effect is strong enough that it actually causes a separation at the trailing edge in the plane of the engine pylon. The wing–body junction separation appears to be unaffected by the presence of the engine.

It became apparent at the Second AIAA Drag Prediction Workshop that a number of CFD codes were overpredicting the lift curve

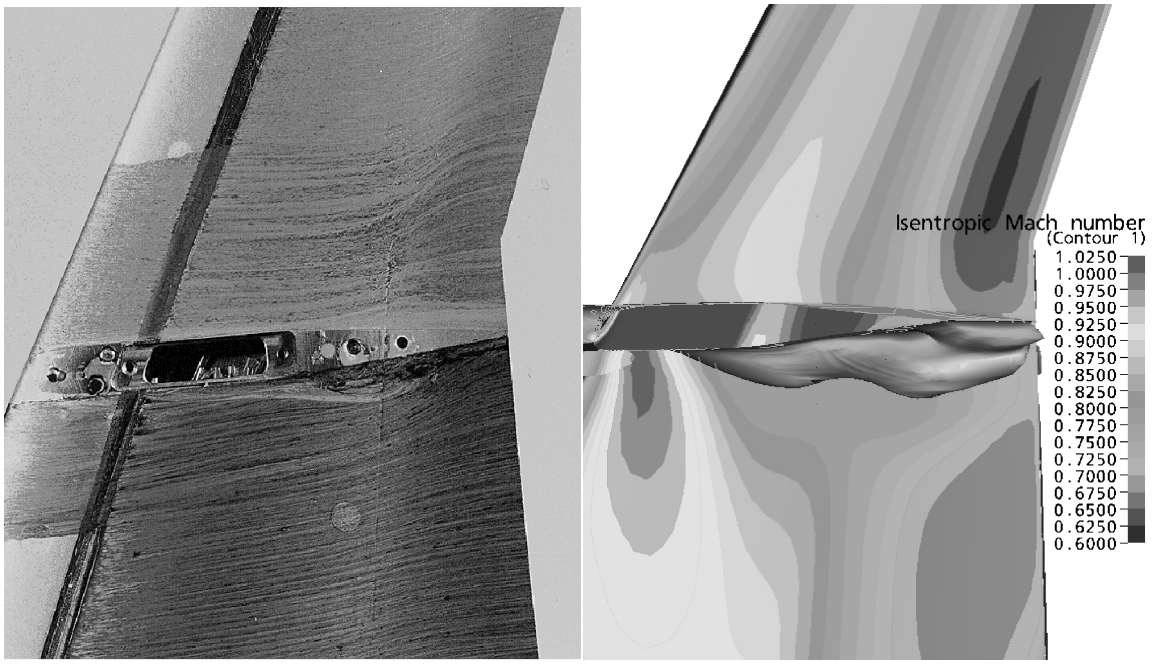

a)

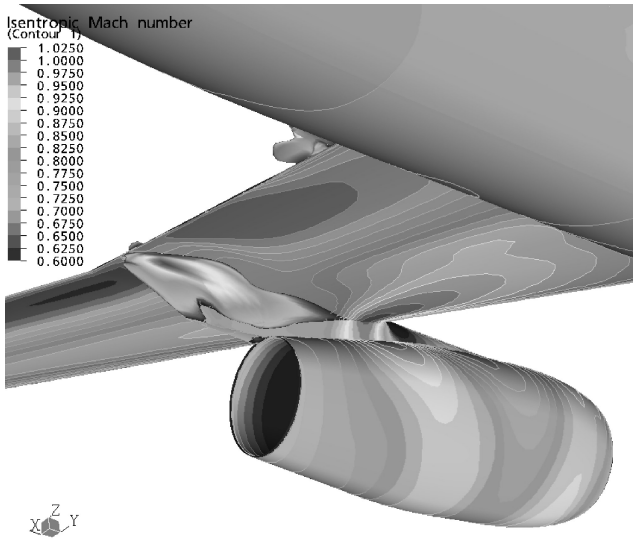

b)

Fig. 9 Comparison between a) experimental oil-flow visualization and b) CFD prediction of wing–engine pylon separation.

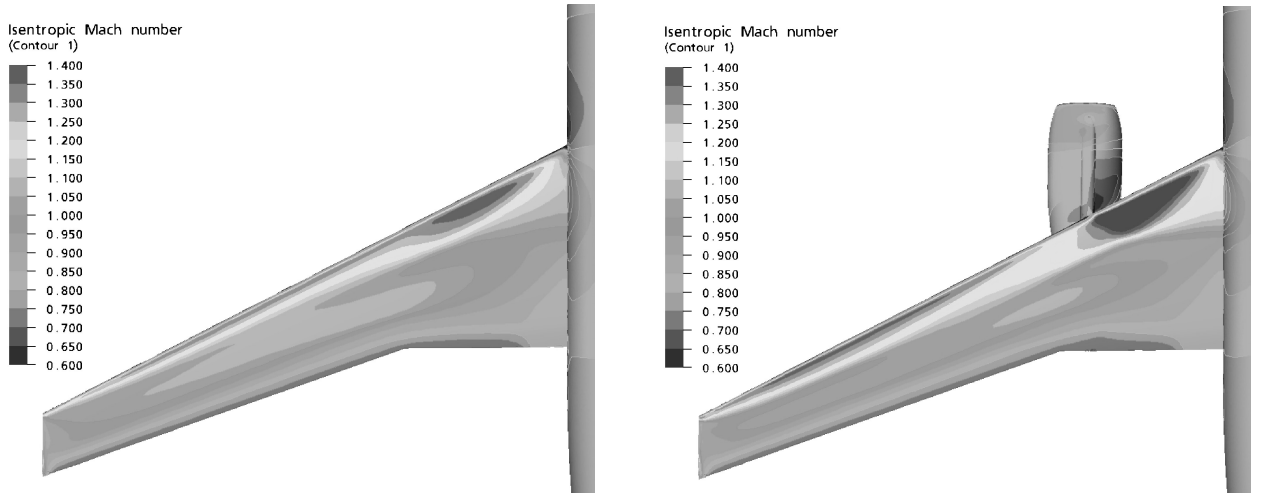

a) b)

Fig. 10 Predicted surface contour of isentropic Mach number for a) WB and b) WBNP configuration.

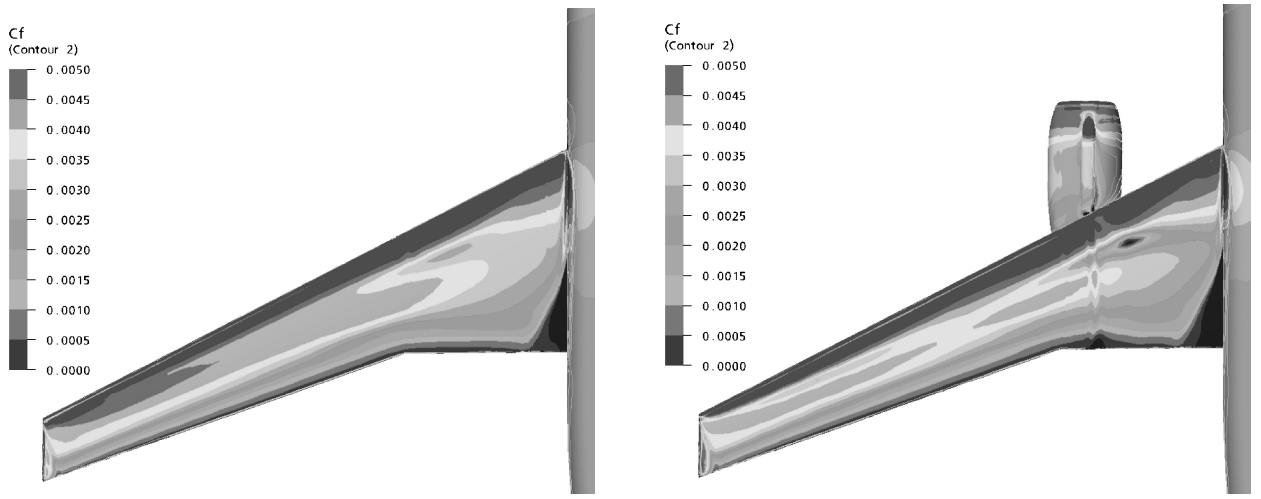

Fig. 11 Predicted surface contour of skin friction *Cf* for a) WB and b) WBNP configuration.

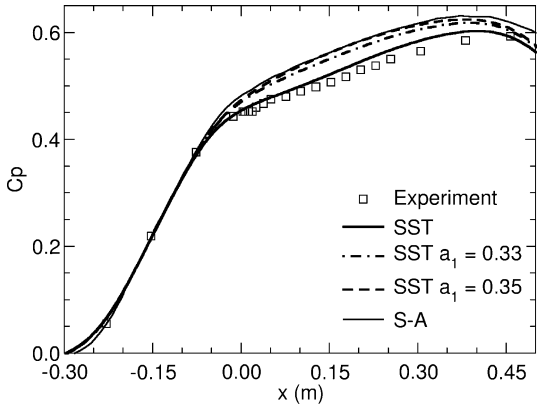

Fig. 12 Wall pressure coefficient *Cp* for Driver's axisymmetric diffuser.[10]

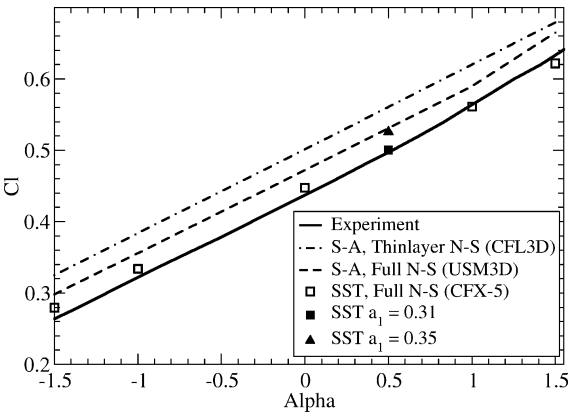

Fig. 13 Effect of thin-layer Navier–Stokes assumption, S–A turbulence model, and SST a_1 constant on computed lift curve slope (*Cl* vs alpha) for WB configuration without engine pylons.

slope, even for the relatively simple configuration without engines. The majority of the computations at the workshop were performed with the one-equation turbulence model of Spalart–Allmaras[9] (S–A). It is known that the S–A model tends to slightly underpredict the amount of separated flow in strong adverse pressure gradients. The SST model on the other hand does a very good job predicting adverse pressure gradient boundary layers. This is shown in Fig. 12 for Driver's axisymmetric diffuser.[10]

The reason the SST model does such a good job of predicting adverse pressure gradient boundary layers is that the standard version of the SST turbulence model includes a modification to the definition of eddy viscosity. This modification is based on Bradshaw's assumption that the turbulent shear stress τ in the boundary layer is proportional to the turbulent kinetic energy k as follows (see Ref. 11):

$$\tau = \rho a_1 k \tag{1}$$

with a_1 being a constant. On the other hand, most one- and two-equation turbulence models define the turbulent shear stress as

$$\tau = \mu_t \frac{\partial u}{\partial y} \tag{2}$$

where $\partial u/\partial y$ is either the shear strain rate S, or the vorticity Ω and μ_t is the eddy viscosity. Equation (2) is known to overpredict the turbulent shear stress in adverse pressure gradients, and as a result, the extent of separation is often underpredicted. To improve the predictions for separated flow, Menter[11] incorporated the Bradshaw assumption into the eddy-viscosity definition of the SST model as follows:

$$\mu_t = \frac{\rho a_1 k}{\max(a_1\omega, F_2 S)} \tag{3}$$

where ω is the turbulence eddy frequency and F_2 is a function that is one for boundary-layer flows and zero for free shear layers.

Also shown in Fig. 12 are the standard SST model results, that is, $a_1 = 0.31$, along with those obtained with the a_1 constant set to 0.33 and 0.35. As the a_1 constant is increased, the effect of the Bradshaw assumption is reduced, and consequently, the size of the separation decreases. The adverse pressure gradient behavior of the SST model is comparable to the S–A model when the a_1 constant is equal to 0.35. To determine whether or not the lift curve slope overprediction observed by many of the participants was caused by these turbulence modeling issues, the effect of the a_1 constant on the DLR-F6 predictions has been investigated.

The lift curve slope obtained by two different Navier–Stokes codes and CFX 5 for the configuration without engines is shown in Fig. 13. The two different codes were included because both used the S–A turbulence model; however, one was a thin-layer and the other was a full Navier–Stokes solver. Also included are the CFX 5 results obtained with the SST constant a_1 equal to 0.35, that is, comparable separation prediction to S–A, and the standard SST value of 0.31.

When the a_1 constant is equal to 0.35, the lift-curve slope is overpredicted by about the same amount as the full Navier–Stokes code with the S–A turbulence model. Figure 14 shows a comparison of

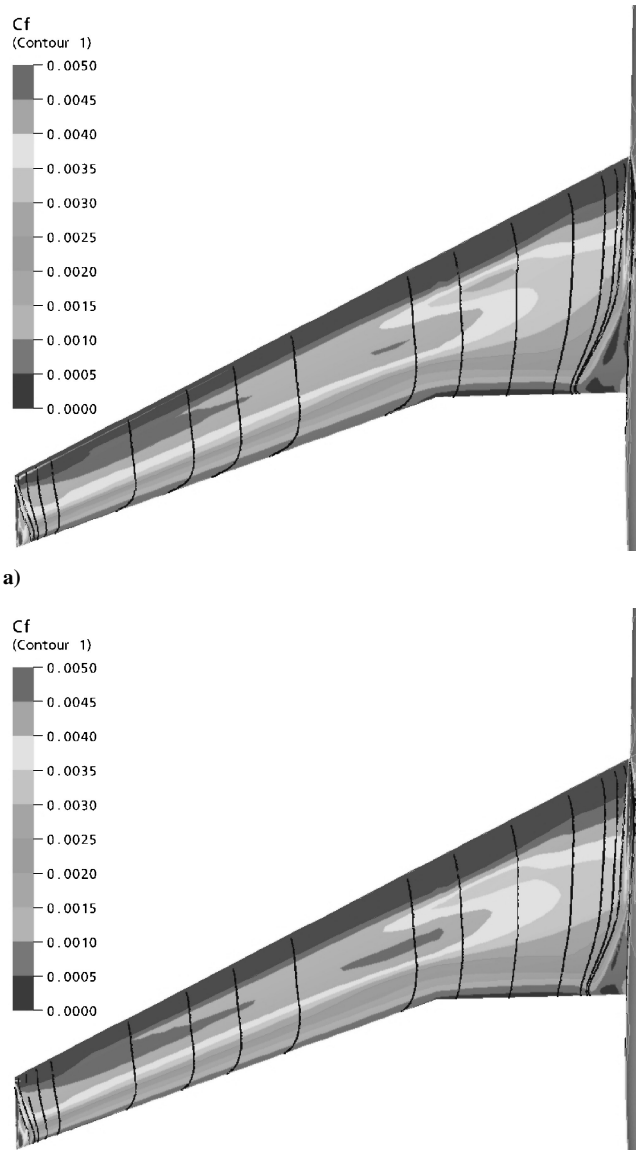

Fig. 14 Predicted surface contour of skin friction *Cf* and surface streamlines for WB configuration with SST a_1 constant equal to standard value of a) 0.31 and b) 0.35.

the absolute value of the wall-shear stress coefficient along with the surface streamlines on the upper wing surface for the simulations with $a_1 = 0.31$ (Fig. 14a) and $a_1 = 0.35$ (Fig. 14b). The main difference is that the separation bubble at the wing–body intersection is reduced and that the trailing-edge wall-shear stress is increased in Fig. 14b. The increase in the trailing-edge wall-shear stress results in less turning of the near-wall boundary-layer flow, which in turn increases the circulation around the wing. As shown in Fig. 14, the trailing-edge flow angle was 47 deg, that is, almost parallel to the trailing edge, for $a_1 = 0.31$ and 36 deg for the $a_1 = 0.35$ case. It is this effect that the present authors believe is responsible for the increased lift predicted by the S–A computations.

The thin-layer simulations reproduced in Fig. 13 show an even stronger shift in the lift curve. Note, however, that a thin-layer approximation[12] can introduce a zero-order error into the viscous term discretization on a nonorthogonal mesh. It is, therefore, not advisable to use that approximation on the type of skewed grids usually generated for complex airframe geometries where often grid angles of 45 deg can be present in corner regions, for example, where the wing meets the fuselage, or the engine pylon meets the wing, both of which had significant separation and viscous effects in this study.

Conclusions

This report has summarized the results obtained by CFX for the Second AIAA Drag Prediction Workshop. The commercial CFD code CFX-5 of ANSYS has been used to compute the engine installation drag for the DLR-F6 aircraft configuration. Good results have been obtained for lift, drag, and pitching moments over a wide range of flight angles of attack. As well, additional computations have indicated that turbulence modeling issues are largely responsible for the overprediction of the lift curve slope that was observed by many of the workshop participants.

Acknowledgments

Part of this work was supported by research grants from the European Union under the FLOMANIA project (Flow Physics Modelling—An Integrated Approach) which is a collaboration between Alenia; ANSYS-CFX; Bombardier; Dassault; EADS-CASA; EADS-Military Aircraft; EDF; NUMECA; DLR, German Aerospace Center; FOI, IMFT, ONERA, Chalmers University, Imperial College, Technical University of Berlin, UMIST and St. Petersburg State University. The project is funded by the European Union and administrated by the CEC, Research Directorate-General, Growth Programme, under Contract G4RD-CT2001-00613.

References

[1]Brodersen, O., and Stürmer, A., "Drag Prediction of Engine-Airframe Interference Effects using Unstructured Navier–Stokes Calculations," AIAA Paper 2001-2414, June 2001.

[2]Raw, M. J., "Robustness of Coupled Algebraic Multigrid for the Navier–Stokes Equations," AIAA Paper 96-0297, Jan. 1996.

[3]Schneider, G. E., and Raw, M. J., "Control Volume Finite-Element Method for Heat Transfer and Fluid Flow Using Collocated Variables," *Computational Procedure. Numerical Heat Transfer*, Vol. 11, No. 4, 1987, pp. 363–390.

[4]Barth, T. J., and Jesperson, D. C., "The Design and Application of Upwind Schemes on Unstructured Meshes," AIAA Paper 89-0366, Jan. 1989.

[5]Rhie, C. M., and Chow, W. L., "Numerical Study of the Turbulent Flow past an Airfoil with Trailing Edge Separation," *AIAA Journal*, Vol. 21, No. 11, 1983, pp. 1525–1532.

[6]Menter, F. R., and Esch, T., "Elements of Industrial Heat Transfer Predictions," *16th Brazilian Congress of Mechanical Engineering (COBEM)*, Uberlandia, Brazil, Nov. 2001.

[7]Grotjans, H., and Menter, F. R., "Wall Functions for General Application CFD Codes," *Proceedings of the 4th Computational Fluid Dynamics Conference*, Vol. 1, Pt. 2, Sept. 1998, pp. 1112–1117.

[8]Levy, D., Zickuhr, T., Vassberg, J., Agrawal, S., Wahls, R., Pirzadeh, S., and Hemsch, M., "Summary of Data from the First AIAA CFD rag Prediction Workshop," AIAA Paper 2002-0841, Jan. 2002.

[9]Spalart, P. R., and Allmaras, S. R., "A One-Equation Turbulence Model for Aerodynamic Flows," *La Recherche Aerospatiale*, Vol. 1, No. 1, 1994, pp. 5–21.

[10]Driver, D. M., "Reynolds Shear Stress Measurements in a Separated Boundary Layer," AIAA Paper 91-1787, June 1991.

[11]Menter, F. R., "Two-Equation Eddy-Viscosity Turbulence Models for Engineering Applications," *AIAA Journal*, Vol. 32, No. 8, 1994, pp. 1598–1605.

[12]Hirsch, C., "Numerical Computation of Internal and External Flows" *Volume 1: Fundamentals of Numerical Discretization*, Wiley, New York, 1988, pp. 63–70.